
This copy is for your personal, non-commercial use only.

If you wish to distribute this article to others, you can order high-quality copies for your colleagues, clients, or customers by [clicking here](#).

Permission to republish or repurpose articles or portions of articles can be obtained by following the guidelines [here](#).

The following resources related to this article are available online at www.sciencemag.org (this information is current as of March 26, 2011):

Updated information and services, including high-resolution figures, can be found in the online version of this article at:

<http://www.sciencemag.org/content/331/6018/757.full.html>

Supporting Online Material can be found at:

<http://www.sciencemag.org/content/suppl/2011/02/08/331.6018.757.DC1.html>

This article **cites 19 articles**, 11 of which can be accessed free:

<http://www.sciencemag.org/content/331/6018/757.full.html#ref-list-1>

This article appears in the following **subject collections**:

Biochemistry

<http://www.sciencemag.org/cgi/collection/biochem>

21. P. J. Scherz, E. McGlenn, S. Nissim, C. J. Tabin, *Dev. Biol.* **308**, 343 (2007).
22. R. Zeller, J. López-Ríos, A. Zuniga, *Nat. Rev. Genet.* **10**, 845 (2009).
23. A. O. Vargas, T. Kohlsdorf, J. F. Fallon, J. Vandenbrooks, G. P. Wagner, *PLoS One* **3**, e3325 (2008).
24. A. Uejima *et al.*, *Dev. Growth Differ.* **52**, 223 (2010).
25. C. Chiang *et al.*, *Dev. Biol.* **236**, 421 (2001).
26. T. Amano, K. Tamura, *Dev. Dyn.* **233**, 326 (2005).
27. M. J. Cohn, C. O. Lovejoy, L. Wolpert, M. I. Coates, *Bioessays* **24**, 460 (2002).
28. J. Zhu *et al.*, *Dev. Cell* **14**, 624 (2008).
29. H. C. Larsson, A. C. Heppleston, R. M. Elsej, *J. Exp. Zool.* **314B**, 571 (2010).
30. A. C. Burke, C. E. Nelson, B. A. Morgan, C. Tabin, *Development* **121**, 333 (1995).
31. T. Suzuki, S. M. Hasso, J. F. Fallon, *Proc. Natl. Acad. Sci. U.S.A.* **105**, 4185 (2008).
32. We thank S. Kuratani for valuable discussions and comments on this study; R. Ladher, J. Fallon, H. Yajima, T. Suzuki, and D. Sipp for critical reading of this manuscript; and Y. Wakamatsu for supplying quail eggs. H.Y. was supported by Grant-in-Aid for Scientific Research on Innovative Areas. This work was supported by

the Global Center of Excellence Program (J03) and grants from Japan Society for the Promotion of Science; the Ministry of Education, Culture, Sports, Science, and Technology of Japan; and the Toray Science Foundation.

Supporting Online Material

www.sciencemag.org/cgi/content/full/331/6018/753/DC1
Materials and Methods
Figs. S1 to S7
References

24 September 2010; accepted 12 January 2011
10.1126/science.1198229

Structure of MyTH4-FERM Domains in Myosin VIIa Tail Bound to Cargo

Lin Wu,* Lifeng Pan,* Zhiyi Wei, Mingjie Zhang†

The unconventional myosin VIIa (MYO7A) is one of the five proteins that form a network of complexes involved in formation of stereocilia. Defects in these proteins cause syndromic deaf-blindness in humans [Usher syndrome I (USH1)]. Many disease-causing mutations occur in myosin tail homology 4—protein 4.1, ezrin, radixin, moesin (MyTH4-FERM) domains in the myosin tail that binds to another USH1 protein, Sans. We report the crystal structure of MYO7A MyTH4-FERM domains in complex with the central domain (CEN) of Sans at 2.8 angstrom resolution. The MyTH4 and FERM domains form an integral structural and functional supramodule binding to two highly conserved segments (CEN1 and 2) of Sans. The MyTH4-FERM/CEN complex structure provides mechanistic explanations for known deafness-causing mutations in MYO7A MyTH4-FERM. The structure will also facilitate mechanistic and functional studies of MyTH4-FERM domains in other myosins.

Mutations in *Myo7a* (also known as *USH1B*), which encodes the unconventional myosin VIIa (MYO7A), cause both syndromic [Usher syndrome I (USH1)] and nonsyndromic (DFNB2 and DFNA11) deafness in humans (1, 2). Although five genes have been associated with USH1 (3–5), mutations of *Myo7a* account for ~40 to 50% of all USH1 cases (2, 6). In vitro studies have shown that the five USH1 proteins (MYO7A, hammonin, cadherin 23, protocadherin 15, and Sans) can form an integrated network of complexes (4, 7–9). Mice containing mutations of any one of the USH1 proteins share common morphological defects in the stereocilia of hair cells (10, 11).

The MYO7A tail contains a pair of myosin tail homology 4—protein 4.1, ezrin, radixin, moesin (MyTH4-FERM) tandems separated by a SH3 domain (a MyTH4-FERM tandem is defined as a MyTH4 domain and a FERM domain arranged right next to each other) (Fig. 1A). Two other unconventional myosins, myosin X and XV, also contain MyTH4-FERM tandem(s) in their tails and play critical roles in the formation of filopodia/stereocilia-like structures as well (10, 12–15). More than 40 missense and 26 deletion/truncation disease-causing mutations are found in the two MYO7A MyTH4-FERM tandems (fig. S1). However, it is not clear why these mutations lead to disease phenotypes, though a recent study has shown that a truncation

mutation in the second MyTH4-FERM tandem of MYO7A decreases the stability of the motor (16).

To elucidate MYO7A-mediated USH1 complex formation, we characterized the interaction between the first MYO7A MyTH4-FERM tandem and Sans, a scaffold protein known to bind to MYO7A (7, 17, 18). Analytical ultracentrifugation shows that the MyTH4-FERM-SH3 region of MYO7A (residues 965 to 1649, referred to as “MFS”) is a stable monomer in solution (Fig. 1C). We confirmed the previous finding by Adato *et al.* (7) that the glutathione *S*-transferase (GST)–fused central domain of Sans [residues 295 to 390, referred to as “CEN” (fig. S2A)] strongly binds to MYO7A-MFS (Fig. 1B). Analytical ultracentrifugation also shows that untagged MYO7A-MFS and Sans CEN form a 1:1 stoichiometric complex in solution (Fig. 1C). We determined the stability of the complex by isothermal titration calorimetry, which gave a dissociation constant (K_d) ~ 50 nM (fig. S2B). Further extension of Sans to the C-terminal end does not change its MYO7A binding affinity (fig. S2D), indicating that Sans CEN encompasses the complete MYO7A binding region.

Nuclear magnetic resonance (NMR) spectra show that the isolated CEN is monomeric and unstructured in solution (fig. S2, E and F). CEN contains highly conserved stretches of residues at each end, separated by a variable connection sequence (fig. S2A). The binding affinities of the two fragments for MYO7A-MFS were K_d ~ 2 μ M for CEN1 (residues 295 to 369) and ~270 μ M for CEN2 (residues 369 to 390) (fig. S2D). Thus, both CEN1 and CEN2 interact directly with MFS, though CEN1 contributes to most of the binding energy. Both CEN1 and

CEN2 are required for the colocalization of MYO7A-MFS and Sans in heterologous cells (fig. S3).

To gain further insight into the MYO7A/Sans interaction, we determined the crystal structure of the MFS/CEN complex at 2.8 Å resolution using a MYO7A isoform containing a 30-residue deletion in its MyTH4 domain (fig. S4 and table S1). This MYO7A-MFS isoform binds to Sans CEN with an affinity indistinguishable from that of MFS containing the 30-residue fragment (fig. S2C). The MYO7A-MFS adopts an overall Y-shaped architecture made up of three domains: (i) the N-terminal MyTH4 domain, (ii) the middle FERM domain, and (iii) the C-terminal SH3 domain (Fig. 1, D and E). The MyTH4 domain directly packs with the FERM F1 lobe, covering ~928 Å² in surface area. The interface is formed by conserved residues that are predominantly polar or charged (fig. S5, A and B).

As expected from its sequence similarity with FERM domains of known structures (19), MYO7A FERM is composed of F1, F2, and F3 lobes, which together form a cloverleaf configuration (Fig. 1D). The SH3 domain is coupled to the F3 lobe by a short α helix (fig. S5C). This hydrophobic α helix packs with the β B/ β A/ β E sheet of the SH3 domain and leaves SH3’s canonical target-recognition pocket open (fig. S5D).

Surprisingly, we could only trace the Sans CEN1 region (residues 305 to 320) in the final complex structure model (Fig. 2A and fig. S6A), though SDS–polyacrylamide gel electrophoresis analysis confirmed the integrity of both MFS and CEN in the complex crystals (fig. S7). The defined CEN1 in the MFS/CEN complex contains 16 conserved residues (Fig. 2). The N-terminal half of CEN1 (residues 305 to 315) adopts a short β hairpin, and the C-terminal half (316 to 320) forms an extended structure (fig. S6B). CEN1 occupies all three interfaces formed between F1, F2, and F3 of the FERM domain and buries a surface area of ~958 Å². The first β strand of the CEN1 hairpin interacts with residues in the F2/F3 interface, the second β strand of the hairpin contacts the residues in the F1/F2 interface, and the last part of CEN1 fills in the F1/F3 gap (Fig. 2). The MFS/CEN1 interaction is different from known recognition modes of FERM domains (fig. S8). The interaction between CEN1 and FERM is mediated by extensive hydrophobic contacts, charge-charge interactions, and hydrogen bonding (Fig. 2B and fig. S9). Supporting the above structural data, the replacement of the conserved Phe³⁰⁷_{CEN1} or Phe³¹⁷_{CEN1} with Glu or the substitution of Phe¹⁴⁷³_{FERM} with

Division of Life Science, Molecular Neuroscience Center, State Key Laboratory of Molecular Neuroscience, Hong Kong University of Science and Technology, Clear Water Bay, Kowloon, Hong Kong.

*These authors contributed equally to this work.

†To whom correspondence should be addressed. E-mail: mzhang@ust.hk

Gln reduced the binding between CEN and MFS (fig. S9B).

The MyTH4 domain adopts a 10-helix bundle architecture. The central six α helices ($\alpha 2$ and $\alpha 5$ to $\alpha 9$), which are highly conserved among various MyTH4 domains (figs. S10 and S11), assemble into a right-handed superhelical core (fig. S12A). The

residues forming the short $\alpha 1$, $\alpha 3$, and $\alpha 4$ helices of MyTH4 domains are more divergent (fig. S11). The final helix ($\alpha 10$) and the $\alpha 9/\alpha 10$ loop are extremely conserved among MyTH4 domains. These two segments cap one end of the six-helix MyTH4 core and make extensive contacts with the FERM F1 lobe to form MyTH4-FERM supramodule

(fig. S5B). The six-helix core of the MyTH4 domain shares some degree of structural similarity with the CID domain of Pcf11, the VHS domain of TOM1, and the ENTH domain of epsinR (fig. S12).

MYO7A MyTH4 contains a prominent exposed hydrophobic pocket comprising the conserved A1189, W1192, I1193, P1220, and Y1223

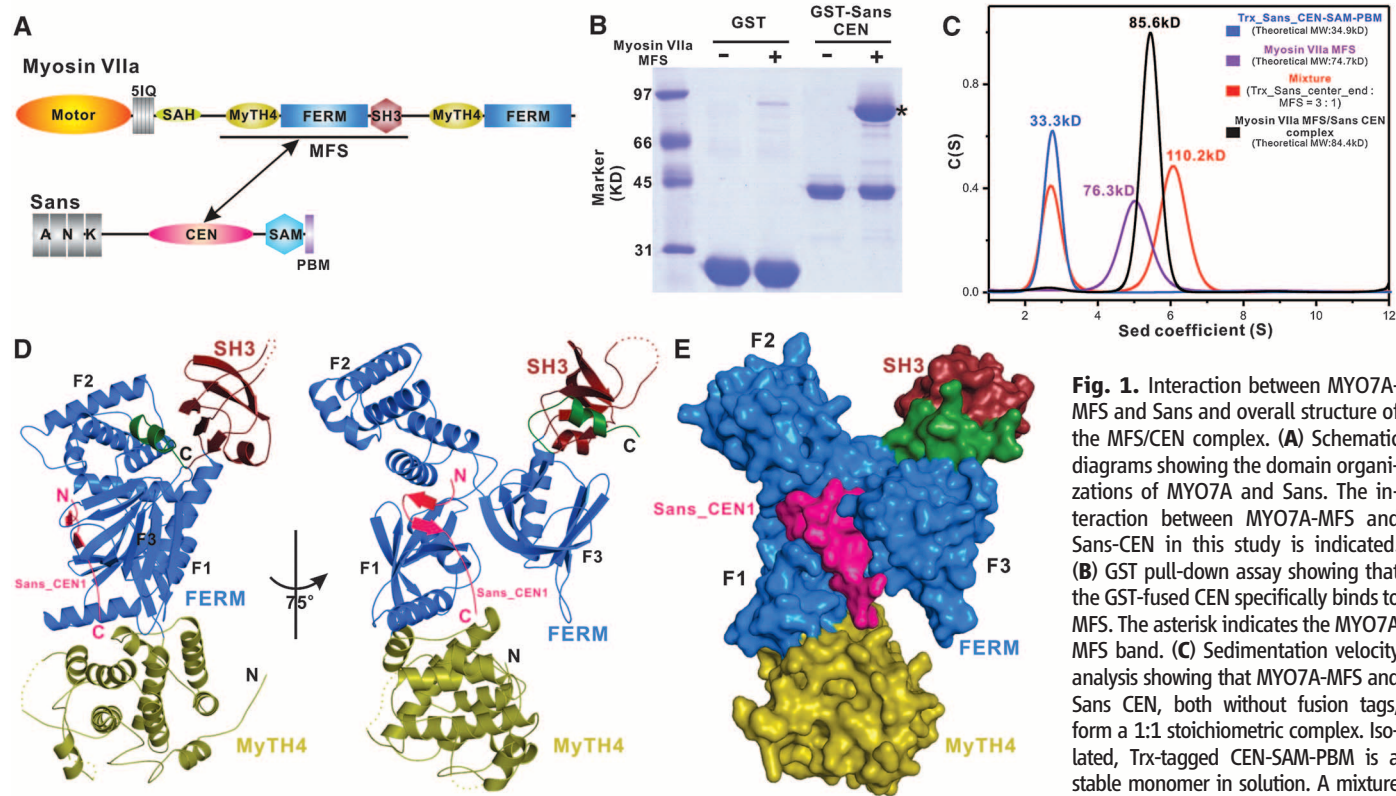


Fig. 1. Interaction between MYO7A-MFS and Sans and overall structure of the MFS/CEN complex. **(A)** Schematic diagrams showing the domain organizations of MYO7A and Sans. The interaction between MYO7A-MFS and Sans-CEN in this study is indicated. **(B)** GST pull-down assay showing that the GST-fused CEN specifically binds to MFS. The asterisk indicates the MYO7A MFS band. **(C)** Sedimentation velocity analysis showing that MYO7A-MFS and Sans CEN, both without fusion tags, form a 1:1 stoichiometric complex. Isolated, Trx-tagged CEN-SAM-PBM is a stable monomer in solution. A mixture of MYO7A-MFS and Trx-CEN-SAM-PBM

at a 3:1 molar ratio gave rise to a complex peak with a molecular mass close to the theoretical value of 109.6 kD for a 1:1 MFS/Trx-CEN-SAM-PBM complex. C(S), sedimentation coefficient distribution; S, Svedbergs. **(D)** Ribbon-diagram representation of the overall structure of the MFS/CEN1 complex. The C-terminal short α helix that integrates the SH3 domain with the FERM domain is shown in green. Two disorder regions in the MyTH4 domain and one in the SH3 domain are indicated by dotted lines. **(E)** Surface representation showing the overall architecture of the MFS/CEN1 complex with the same coloring scheme as in (D).

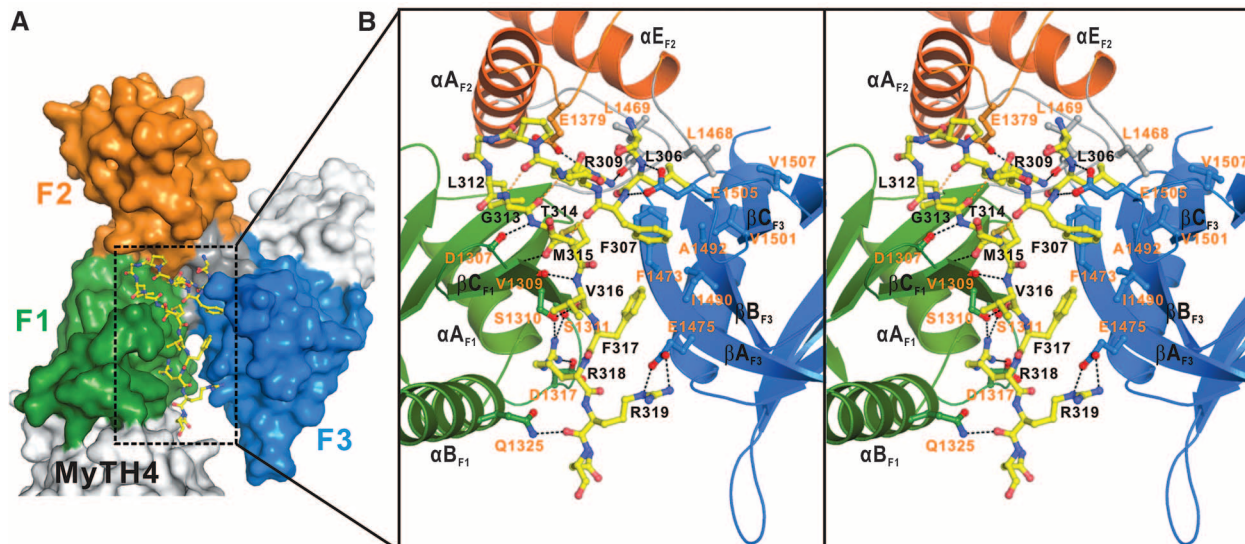


Fig. 2. Detail of the MFS/CEN1 interaction. **(A)** Surface representation showing the binding interface between the FERM domain of MFS and CEN1. The F1, F2, F3 lobes of FERM are in direct contact with CEN1 (shown in explicit atomic model). **(B)** Stereo view showing the detailed interactions between FERM and CEN1.

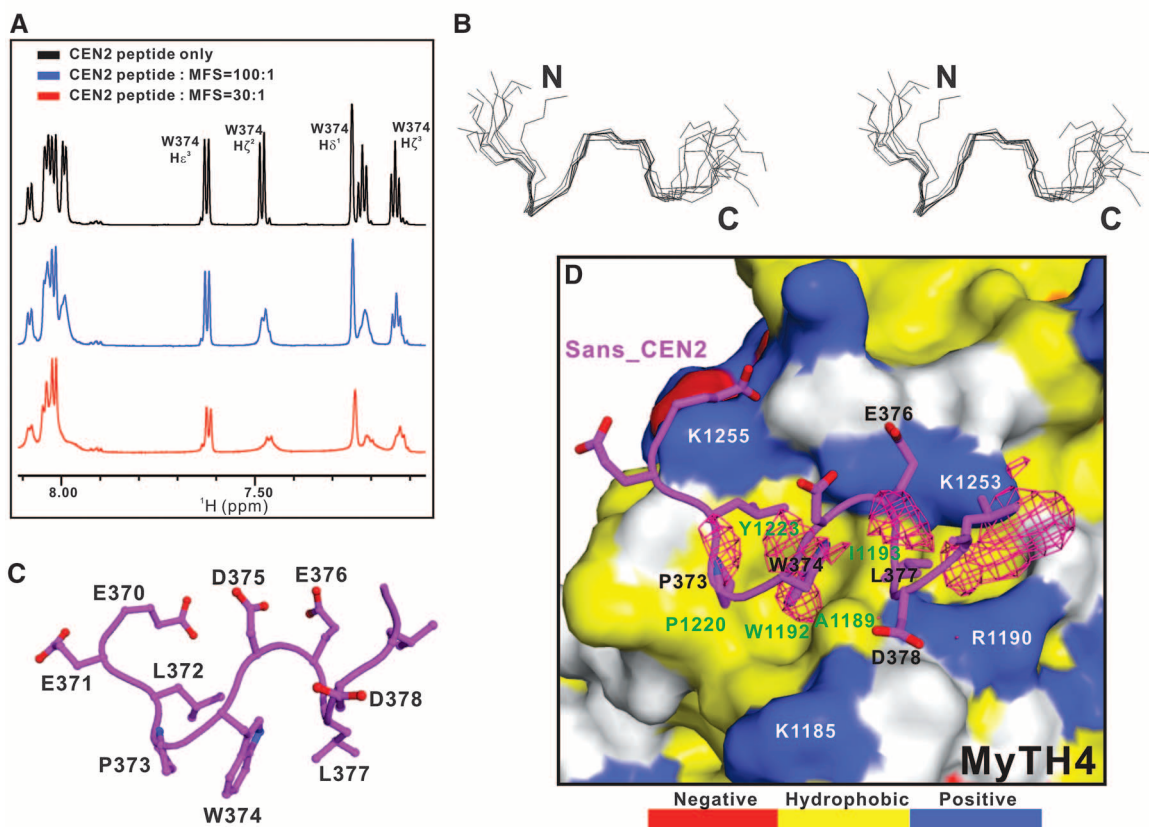
residues (Fig. 3D and fig. S13A) (20). The rim of this hydrophobic surface is decorated by four conserved, positively charged residues (K1255, K1253, R1190, and K1185) (Fig. 3D and fig. S13B). This hydrophobic surface is fully accessible (that is, not influenced by the crystal packing) (fig. S14). Interestingly, some sparse electron densities that

do not belong to MYO7A-MFS can be observed on this surface (fig. S13B). The Sans CEN2 is negatively charged and contains several conserved hydrophobic residues (fig. S2A), suggesting that CEN2 may directly bind to the MyTH4 domain of MYO7A. This analysis is supported by the observation that substitution of A1189 in the hy-

drophobic pocket of MyTH4 with Glu leads to a ~10-fold decrease of the binding affinity between MFS and CEN (fig. S13C). Conversely, substitution of W374 with Gln in CEN2 also weakens the MFS/CEN interaction by ~10-fold (fig. S13D). However, the poor-density map prevented us from modeling the CEN2 structure in the complex.

Fig. 3. The MyTH4/CEN2 interaction.

(A) The aromatic and amide region of the CEN2 peptide ¹H-NMR spectra with increasing molar ratios of MYO7A-MFS, ppm, parts per million. (B) Stereo view showing the backbones of the superimposed final 10 NMR structures of the CEN2 peptide (residues 370 to 380). (C) The combined stick model and the ribbon representation showing a representative NMR structure of the MFS-bound CEN2 peptide. (D) Surface representation showing the binding interface between the CEN2 peptide and the MyTH4 domain. In this presentation, the hydrophobic amino acid residues in MyTH4 surface model are shown in yellow, positively charged residues in blue, negatively charged residues in red, and uncharged polar residues in gray.



The sparse electron densities of the MyTH4 domain in the MFS/CEN complex are shown. The F_0-F_C density map is contoured at 2.5σ .

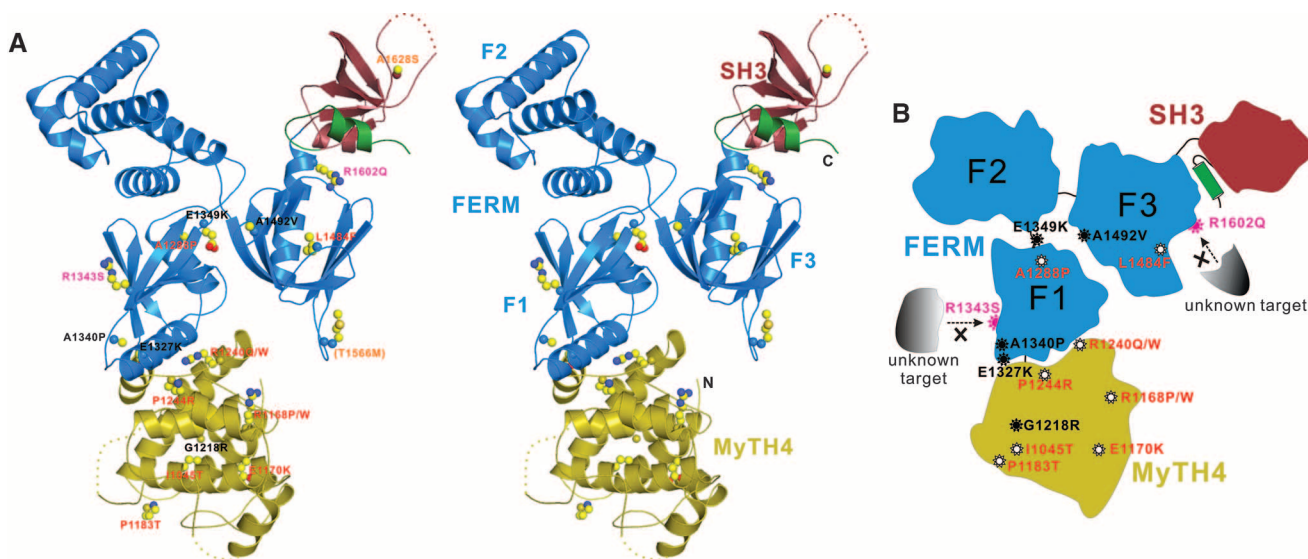


Fig. 4. Missense mutations in MYO7A-MFS found in human patients. (A) Combined stick-dot model and ribbon-diagram representations in stereo view showing the distributions of the 17 missense mutation sites in MFS. The residues in the mutation sites are labeled in red, orange, pink, and

black corresponding to the classes I to IV described in the text, respectively. (B) Schematic cartoon summarizing the 17 missense mutations of MYO7-MFS. The \times marks denote mutations that may disrupt unknown target binding.

We used NMR spectroscopy to interrogate binding between MyTH4 and CEN2. A 21-residue synthetic peptide corresponding to CEN2 was confirmed to bind to MFS using the transferred nuclear Overhauser effect (NOE) technique (Fig. 3A and fig. S15). We determined the structure of the MFS-bound CEN2 with the use of transferred NOE-derived distance restraints (Fig. 3B and table S2). A seven-residue fragment (372 to 378) of CEN2 adopts a defined conformation, with the aromatic ring of W374 sandwiched by P373, L372, and L377, forming a hydrophobic cluster. The opposite face of this hydrophobic cluster contains five negatively charged residues (Fig. 3C). The CEN2 NMR structure was docked to the MyTH4 domain using the program HADDOCK (21). The final docked structure reveals a good surface match between CEN2 and MyTH4, and the CEN2 peptide fits reasonably well with the unexplained electron densities observed in MyTH4 (Fig. 3D). Together with the cellular imaging data (fig. S3), we conclude that CEN2 contributes to the overall binding between MFS and CEN.

A total of 19 missense mutations involving 17 amino acids within MYO7A-MFS have been documented in Usher syndrome patients (fig. S1). The distribution of the 17 missense variants is mapped onto the structure of MFS (Fig. 4; truncation/deletion mutations are not discussed here as these can be interpreted as null mutations). Among the 17 mutation sites, 7 are in MyTH4, 9 in FERM, and 1 in SH3 (Fig. 4B). These 17 MYO7A-MFS variants can be divided into four classes (fig. S16): The first class of the mutations occurs in the folding core of the MyTH4 domain [Ile¹⁰⁴⁵→Thr¹⁰⁴⁵ (I1045T), R1168P/W, E1170K, P1183T, R1240Q/W, and P1244R] or the FERM domain (A1288P in F1 and L1484F in F3) (Fig. 4 and fig. S16A). The disease-causing mutations in this category are likely to have a deleterious impact on the folding of the MyTH4-FERM supramodule. The mutations in the second class (G1218K in MyTH4; E1327K, A1340P, and E1349K in F1; A1492V in F3) may not affect the structure of the individual domains but instead are likely to interfere with the interdomain interactions

or the interaction between MYO7A and Sans, as these residues are situated in the interface between the domains, as well as in the interface between MFS and Sans CEN (Fig. 4 and fig. S16B). For example, E1349 is intimately involved in binding to Sans CEN1; the E1349K-MFS mutation weakens its Sans binding by ~20-fold (fig. S2D). The third class of mutants involves the conserved R1343 in F1 and R1602 in F3. Both of these residues are solvent-exposed and not expected to play obvious structural roles in MFS folding or in Sans binding, but they may affect interactions between MYO7A-MFS and its other partners (Fig. 4 and fig. S16C). The fourth class of mutations (T1566M and A1628S) cannot be interpreted by the MFS/CEN structure.

Structure-based sequence analysis indicates that the supramodular nature is probably a general property of other MyTH4-FERM tandems (fig. S10). In the MYO7A-MFS, $\alpha 9$, $\alpha 10$, and the $\alpha 9/\alpha 10$ loop of MyTH4 form the MyTH4/FERM interface (fig. S5B). The $\alpha 9/\alpha 10$ loop and $\alpha 10$ contain a conserved R-X-X-X-P-X-(X)-X-E motif in all MyTH4 domains (fig. S11). The Arg and Glu residues in this motif form a salt bridge to define the orientation of $\alpha 9$ and $\alpha 10$, and the Pro residue (P1244) facilitates the formation of the turn structure in the $\alpha 9/\alpha 10$ loop (Fig. 4A). Mutations of Arg or Pro residue in this signature motif of either of the MYO7A MyTH4-FERM tandems cause deaf-blindness in humans (fig. S10). The supramodular structure of MYO7A-MFS also correlates well with the observation that MyTH4 domains invariably coexist with FERM domains in MyTH4-containing proteins. Finally, sequence-alignment analysis further predicts that the majority of the disease-causing mutations in the second MYO7A MyTH4-FERM tandem would either disrupt the folding of the domains or cripple the inter-MyTH4-FERM interface (fig. S10). The MYO7A-MFS structure not only provides mechanistic explanations to currently known disease-causing mutations in the MYO7A MyTH4-FERM tandems, but it will also be valuable in understanding functions of other MyTH4-FERM containing myosins.

References and Notes

1. S. Riazuddin *et al.*, *Hum. Mutat.* **29**, 502 (2008).
2. T. Jaijo *et al.*, *J. Med. Genet.* **44**, e71 (2007).
3. J. Reiners, U. Wolfrum, *Adv. Exp. Med. Biol.* **572**, 349 (2006).
4. A. El-Amraoui, C. Petit, *J. Cell Sci.* **118**, 4593 (2005).
5. Z. M. Ahmed, S. Riazuddin, S. Riazuddin, E. R. Wilcox, *Clin. Genet.* **63**, 431 (2003).
6. X. M. Ouyang *et al.*, *Hum. Genet.* **116**, 292 (2005).
7. A. Adato *et al.*, *Hum. Mol. Genet.* **14**, 347 (2005).
8. B. Boëda *et al.*, *EMBO J.* **21**, 6689 (2002).
9. J. Siemens *et al.*, *Proc. Natl. Acad. Sci. U.S.A.* **99**, 14946 (2002).
10. G. Lefèvre *et al.*, *Development* **135**, 1427 (2008).
11. M. Schwander, B. Kachar, U. Müller, *J. Cell Biol.* **190**, 9 (2010).
12. A. Wang *et al.*, *Science* **280**, 1447 (1998).
13. F. J. Probst *et al.*, *Science* **280**, 1444 (1998).
14. D. Well *et al.*, *Nature* **374**, 60 (1995).
15. T. Self *et al.*, *Development* **125**, 557 (1998).
16. M. Schwander *et al.*, *J. Neurosci.* **29**, 15810 (2009).
17. D. Weil *et al.*, *Hum. Mol. Genet.* **12**, 463 (2003).
18. Materials and methods are available as supporting material on Science Online.
19. U. Tepass, *Curr. Opin. Genet. Dev.* **19**, 357 (2009).
20. Single-letter abbreviations for the amino acid residues are as follows: A, Ala; C, Cys; D, Asp; E, Glu; F, Phe; G, Gly; H, His; I, Ile; K, Lys; L, Leu; M, Met; N, Asn; P, Pro; Q, Gln; R, Arg; S, Ser; T, Thr; V, Val; W, Trp; Y, Tyr; and X, any amino acid.
21. C. Dominguez, R. Boelen, A. M. Bonvin, *J. Am. Chem. Soc.* **125**, 1731 (2003).
22. We thank T. Friedman for providing the mouse MYO7A cDNA construct, J. Yu and Y. Shang for the help in crystallography, Y. Zhao for the in-house x-ray diffractor, the BL17U1 of the Shanghai Synchrotron Radiation Facility for the beamline time, and A. Zhang for reading the manuscript. This work was supported by grants from the Research Grant Council of Hong Kong to M.Z. (663808, 664009, 663610, CA07/08.SCO1, SEG_HKUST06, and AoE/B-15/01-II). The atomic coordinates and structure factors of the complex structure have been deposited in the Protein Data Bank under the accession code 3PVL. The superimposed final 10 NMR structures of the CEN2 peptide have been deposited in the Protein Data Bank under the accession code 2L7T.

Supporting Online Material

www.sciencemag.org/cgi/content/full/331/6018/757/DC1
Materials and Methods
Figs. S1 to S16
Tables S1 and S2
References

8 October 2010; accepted 3 January 2011
10.1126/science.1198848

HSPC117 Is the Essential Subunit of a Human tRNA Splicing Ligase Complex

Johannes Popow,^{1*} Markus Englert,^{2*} Stefan Weitzer,¹ Alexander Schleiffer,³ Beata Mierzwa,¹ Karl Mechtler,⁴ Simon Trowitzsch,^{5†} Cindy L. Will,⁵ Reinhard Lührmann,⁵ Dieter Söll,^{2,6‡} Javier Martinez^{1,‡}

Splicing of mammalian precursor transfer RNA (tRNA) molecules involves two enzymatic steps. First, intron removal by the tRNA splicing endonuclease generates separate 5' and 3' exons. In animals, the second step predominantly entails direct exon ligation by an elusive RNA ligase. Using activity-guided purification of tRNA ligase from HeLa cell extracts, we identified HSPC117, a member of the UPF0027 (RtcB) family, as the essential subunit of a tRNA ligase complex. RNA interference-mediated depletion of HSPC117 inhibited maturation of intron-containing pre-tRNA both in vitro and in living cells. The high sequence conservation of HSPC117/RtcB proteins is suggestive of RNA ligase roles of this protein family in various organisms.

Transfer RNAs (tRNAs) are essential adaptor molecules in the translation of the genetic transcript into proteins. During their post-

transcriptional maturation (*I*), intron-containing tRNA precursor transcripts (pre-tRNAs) undergo splicing, which is accomplished by a specialized

endonuclease that excises the intron (2, 3) and a ligase that joins the resulting exon halves (fig. S1A). Although introns within pre-tRNA transcripts have been detected in all domains of life,

¹Institute of Molecular Biotechnology of the Austrian Academy of Sciences (IMBA), A-1030 Vienna, Austria. ²Department of Molecular Biophysics and Biochemistry, Yale University, New Haven, CT 06520, USA. ³Bioinformatics Department, Research Institute of Molecular Pathology (IMP)-IMBA, A-1030 Vienna, Austria. ⁴Protein Chemistry Department, Research Institute of Molecular Pathology (IMP)-IMBA, A-1030 Vienna, Austria. ⁵Department of Cellular Biochemistry, Max Planck Institute for Biophysical Chemistry, 37077 Göttingen, Germany. ⁶Department of Chemistry, Yale University, New Haven, CT 06520, USA.

*These authors contributed equally to this work.

†Present address: European Molecular Biology Laboratory, Grenoble Outstation, and Unit of Virus Host Cell Interactions, UMI3265, Grenoble Cedex 9, France.

‡To whom correspondence should be addressed. E-mail: javier.martinez@imba.oew.ac.at (J.M.); dieter.soll@yale.edu (D.S.)